

Kinetically Controlled Synthesis of Metallic Glass Nanoparticles with Expanded Phase Space

Bing Deng,^{1,#,*} Zhe Wang,^{1,#,†} Zhen-Yu Wu,^{2,#} Lu Ma,³ Chi Hun Choi,⁴ Gang Li,¹ Zhe Yuan,¹ Jinhang Chen,¹ Duy Xuan Luong,^{1,5} Lucas Eddy,^{1,5} Bongki Shin,⁴ Alexander Lathem,^{1,5} Weiyin Chen,¹ Yi Cheng,¹ Yimo Han,⁴ Boris I. Yakobson,^{1,4,6} Haotian Wang,^{1,2,4,*} Yufeng Zhao,^{7,*} and James M. Tour^{1,4,6,8,*}

¹ Department of Chemistry, Rice University, Houston, TX 77005, USA

² Department of Chemical and Biomolecular Engineering, Rice University, Houston, TX 77005, USA

³ National Synchrotron Light Source II (NSLS-II), Brookhaven National Laboratory, Upton, NY 11973, USA

⁴ Department of Materials Science and NanoEngineering, Rice University, Houston, TX 77005, USA

⁵ Applied Physics Program, Rice University, Houston, TX 77005, USA

⁶ Smalley-Curl Institute, Rice University, Houston, TX 77005, USA

⁷ Corban University, 5000 Deer Park Drive SE, Salem, OR 97317, USA

⁸ NanoCarbon Center and the Welch Institute for Advanced Materials, Rice University, Houston, TX 77005, USA

† Present address: Department of Chemistry, Northwestern University, Evanston, IL 60208, USA

These authors contributed equally.

*Corresponding authors: J.M.T. (tour@rice.edu), Y.Z. (YZhao@corban.edu), H.T.W.

(htwang@rice.edu), B.D. (bingdeng@rice.edu)

Abstract

Nanoscale metallic glasses offer opportunities for investigating fundamental properties of amorphous solids and technological applications in biomedicine, microengineering, and catalysis. However, the top-down fabrication of metallic glass nanostructure is restricted by the availability of bulk metallic glass; in contrast, the bottom-up synthesis remains rarely explored due to the rigorous formation conditions, especially the extreme cooling rate. Here we develop a kinetically controlled flash carbothermic reaction, featuring ultrafast heating and cooling rates, for the synthesis of metallic glass nanoparticles within milliseconds. Ten permutations of noble metals, base metals, and metalloid (M_1 - M_2 -P, $M_1 = \text{Pt/Pd}$, $M_2 = \text{Cu/Ni/Fe/Co/Sn}$) were synthesized with widely tunable particle sizes and supportive substrates. Through combinatorial development, we discovered a substantially expanded phase space for metallic glass at the nanoscale than that at the bulk scale, revealing an enhanced glass forming ability due to the nanosize effect. Leveraging this effect, we synthesized several nanoscale metallic glasses with elemental compositions that have never, to our knowledge, been synthesized in bulk. The metallic glass nanoparticles show high intrinsic activity in electrocatalysis and heterogeneous catalysis, outperforming crystalline nanoparticle counterparts and commercial precious metal nanoparticle benchmarks.

Introduction

Metallic glasses (MG), first discovered through melt quenching of the Au-Si alloy¹, are a broad class of solid metallic materials with amorphous atomic structures². Depending on their glass forming ability (GFA), which is quantitatively described by the critical cooling rate (R_C), MG exhibit many dimensional forms that are accessible using varied fabrication methods. For example, MG ribbons, typically $<100 \mu\text{m}$, are made by rapid quenching of alloy melts¹, MG thin films are

fabricated by physical vapor deposition^{3,4}, and bulk MG with very low R_C are afforded by casting^{5,6}. Recently, MG nanostructures have received considerable interests due to their unique atomic structures⁷, intriguing properties like size-dependent mechanics⁸⁻¹⁰, and the opportunities to extend their use into unconventional areas including additive manufacturing¹¹, nanoimprinting¹², and catalysis¹³⁻¹⁷. The present top-down fabrication of MG nanostructures involves thermoplastic forming using nanomolds^{12,16,18}, thermal drawing techniques¹⁹, selective etching²⁰, and laser ablation in liquids²¹. However, the top-down approaches rely on the availability of a bulk MG counterpart, which heavily restricts the materials and composition choice. In contrast, several bottom-up methods for nanoscale MG synthesis have been reported recently, including chemical reduction^{8,22-24}, electrochemical synthesis^{13,25}, and physical vapor deposition²⁶, affording better size, morphology, and compositional tunability. However, wet chemistry-based processes often lead to contamination by surfactants²⁴, while physical deposition methods require a substrate that hinders intrinsic property studies and wide-range applications. It is highly desired but still challenging to develop a bottom-up method for the synthesis of nanoscale MG with pure and tunable compositions, as well as small size and good morphology.

A thermal process for bottom-up synthesis of nanoscale MG necessitates certain features. First, a high temperature is necessary to ensure the intimate mixing of multiple metal elements with diverse miscibility, as MG are typically composed of three or more elements (ref²). Secondly, a short reaction duration is required to minimize particle agglomeration and achieve uniform, nanoscale particle dispersion. Lastly, an ultrafast cooling rate is needed to vitrify the alloy melt and avoid crystallization. Recently, several unconventional thermal processes have been reported for synthesis of alloy nanoparticles with single-phase crystal structures, such as the electrothermal-based shock synthesis of high-entropy alloy nanoparticles^{27,28} and intermetallic nanoparticles²⁹,

and the photothermal-based laser ablation synthesis of high-entropy alloy and ceramic nanoparticles³⁰. We anticipate that by rational composition design, nonequilibrium thermal processes can kinetically suppress crystallization and produce metastable glassy materials.

In this context, we here report the flash carbothermic reaction (FCR) for the general synthesis of metallic glass nanoparticles (MGNP). Metal precursors loaded on a carbon substrate are subjected to millisecond current pulses, rapidly raising the temperature to ~ 1800 K through Joule heating ($>10^5$ K s⁻¹). The resulting alloy melts then cool at an ultrafast rate ($>10^4$ K s⁻¹) through thermal radiation, vitrifying into glassy nanoparticles. FCR is feasible for the synthesis of various Pd- and Pt-based MGNP, including PdNiP, PdCuP, PdCuNiP, PtNiP, PtCuP, PtCuNiP, and the high-entropy PtPdCuNiP. By constructing the phase diagram of PdNiP nanoparticles through combinational development, we discover that the phase space of MG at the nanoscale is substantially expanded than that of the bulk counterpart, implying that the nanosize effect enhances the GFA. *Ab initio* calculations further reveal delicate short-range order differences between nanoscale and bulk MG. Importantly, the enhanced GFA allows for the synthesis of nanoscale MG with compositions that have yet to be achieved in bulk, exemplified by PdCoP, PdSnP, and the high-entropy PdCuFeNiP. Furthermore, we demonstrated the application of the PtNiP MGNP for electrocatalytic hydrogen evolution, which outperforms crystalline nanoparticles and the commercial Pt/C benchmark.

Synthesis of PdNiP MGNP by flash carbothermic reaction

The FCR for MGNP synthesis involves three steps. First, metal/metalloid precursors were dissolved in ethanol and homogeneously impregnated onto a carbon black support, which served as both a conductive additive and a supporting substrate (Supplementary Fig. 1). Structurally,

carbon black consists of amorphous carbon nanospheres (Supplementary Fig. 2). Second, pulsed direct current input rapidly raises the temperature of the sample^{27,31}, leading to the decomposition of the metal precursors and subsequent fusion into alloy melts (Fig. 1a). Finally, the sample was rapidly cooled due to the intensive thermal radiation and low heat capacity ($<0.033 \text{ J K}^{-1}$, ref³²) of the carbon substrate (Fig. 1a), resulting in the vitrification of the alloy melt into glassy nanoparticles (Fig. 1b). Due to the good GFA, the ternary palladium-nickel-phosphorous (PdNiP) alloy was chosen for the initial trials⁶. In a typical experiment, a pulsed current of $\sim 90 \text{ A}$ within 50 ms was applied to the precursor mixture in an Ar-filled chamber (Fig. 1c, Supplementary Fig. 3). The sample exhibited strong light emission (Fig. 1c, inset), and the real-time temperature was measured using a pyrometer (Fig. 1d). The temperature rapidly reached its maximum at $T_{\text{max}} \sim 1760 \text{ K}$, beyond the decomposition temperature of the metal precursors (Supplementary Table 1). Based on T_{max} and the glass transition temperature (T_{g}) of PdNiP MG ($\sim 600 \text{ K}$)^{33,34}, the cooling rate was calculated to be $\sim 1.5 \times 10^4 \text{ K s}^{-1}$, which is higher than the R_{C} of PdNiP bulk MG³⁵.

The amorphous structure of the as-obtained PdNiP NP was confirmed by X-ray diffraction (XRD) and transmission electron microscopy (TEM). The XRD pattern did not show any peaks from crystalline components, except for the broad diffraction peaks from the amorphous carbon support (Fig. 1e). The as-synthesized NP are supported on carbon black (Fig. 1f), with an average particle size of $\sim 10.6 \text{ nm}$ and a narrow size distribution (Supplementary Fig. 4). The selected-area electron diffraction (SAED) shows diffusive diffraction halos without discrete spots (Fig. 1f, inset). The amorphous structure of the PdNiP MGNP was further confirmed by high-resolution TEM (HRTEM) and the corresponding fast Fourier transformation (FFT) pattern (Fig. 1g). HRTEM images with tilt range from 0° to 5° were acquired and all characterized the product as an amorphous structure (Supplementary Fig. 5). To exclude the effect of the carbon support,

nanobeam diffraction was performed on a single NP, which showed similar diffuse halos typical of an amorphous structure (Fig. 1h). The normalized intensity of the nanobeam diffraction pattern showed the main peak positions at 4.12 nm^{-1} and 6.96 nm^{-1} , corresponding to $k_2/k_1 \sim 1.69$ (Fig. 1h), in agreement with previous experimental results on PdNiP bulk MG³⁶.

The average composition of the MGNP was determined to be $\text{Pd}_{43}\text{Ni}_{26}\text{P}_{31}$ by energy-dispersive X-ray spectroscopy (EDS) (Supplementary Note 1, Supplementary Fig. 6). High-angle annular dark-field scanning transmission electron microscopy (HAADF-STEM) image and element maps demonstrated uniform distributions of Pd, Ni, and P in the MGNP (Fig. 2a). We investigated the electronic structures of the PdNiP MGNP by X-ray photoemission spectroscopy (XPS) (Supplementary Note 2, Supplementary Fig. 7, Supplementary Table 3). Various chemical bonds, including Pd-Pd, Ni-Ni, P-P, Pd-Ni, Pd-P and Ni-P, were found in the PdNiP MGNP, resulted from its amorphous feature.

General synthesis of Pd- and Pt-based metallic glass nanoparticles

To demonstrate the versatility of our FCR method, a series of Pd- and Pt-based MGNP were synthesized (Fig. 2, Supplementary Table 2). Typically, the GFA of an alloy is susceptible to its composition, where even the difference of a few atomic ratio percentages could induce a change of R_C by several orders of magnitude³⁷. Nevertheless, due to the presence of deep eutectics in the Pd-P and Pt-P systems, Pd- and Pt-based MG can be synthesized over a wide compositional range³⁸. To control product composition, we employed an excessive supply of P, given its higher volatility compared to other metal components (Supplementary Tables 1-2). The amorphous features of the synthesized nanoparticles were confirmed through multiscale characterization methods, including XRD, SAED, and HRTEM. The average compositions were $\text{Pd}_{43}\text{Ni}_{26}\text{P}_{31}$ (Fig.

2a), Pd₄₈Cu₃₀P₂₂ (Fig. 2b, Supplementary Figs. 8-10), Pd₄₉Cu₁₃Ni₈P₃₀ (Fig. 2c, Supplementary Figs. 11-13), Pt₃₄Ni₄₄P₂₂ (Fig. 2d, Supplementary Figs. 14-16), Pt₃₄Cu₃₈P₂₈ (Fig. 2e, Supplementary Figs. 17-19), Pt₄₈Cu₁₄Ni₁₁P₂₇ (Fig. 2f, Supplementary Figs. 20-22), and the quinary Pt₂₁Pd₃₂Cu₁₁Ni₉P₂₇ (Fig. 2g, Supplementary Figs. 23-25), which is considered a high-entropy MG^{13,39,40}. The atomic resolution HAADF-STEM of a typical PtPdCuNiP nanoparticle further proved the amorphous structure (Fig. 2h). The nanoparticles exhibited structural and elemental uniformity, regardless of their compositions (Fig. 2i).

The FCR method for MGNP synthesis offers wide tunability in terms of particle size, dispersity, composition, and substrate. The MGNP show a narrow size distribution with a coefficient of variation <10%, and the particle size can be adjusted from 5 to 100 nm by varying precursor loading (Supplementary Fig. 26). The as-synthesized MGNP were uniformly dispersed on the carbon black support, and other conductive carbons like carbon nanotubes can also be used (Supplementary Fig. 27), expanding the range of substrate applicability. Importantly, the MGNP remained stable in atmospheric conditions at room temperature and preserve their structure, size, and morphology even after 6 months of storage (Supplementary Fig. 28). The FCR process for MGNP synthesis is also scalable. By simply increasing the FCR voltage, we achieved a batch size of 0.2 g (Supplementary Note 3, Supplementary Fig. 29). Given the short duration per batch (~50 ms), the FCR process could enable scalable MGNP production for a wide range of applications.

Kinetically controlled synthesis by ultrafast cooling

We conducted controlled experiments to explore the formation mechanism of MGNP using FCR. Deviating from thermodynamically equilibrium crystal phases, metallic glass is typically trapped by a kinetic barrier. We examined the effect of FCR time on MGNP formation using the same Pt-

Ni-P precursors for durations of 50, 100, and 150 ms. With an increase in time to ≥ 100 ms, crystal peaks emerged (Fig. 3a), and the particle sizes grew larger (Fig. 3b). Nanoparticles synthesized for 50 ms were amorphous (Fig. 3c). As the duration increased to 100 ms, we observed the coexistence of partially and fully crystallized nanoparticles (Fig. 3d, Supplementary Fig. 30). The lattice fringes suggested the formation of crystal phases, such as NiP₂(210) with interplanar spacing of $d = 2.36$ Å and PtP₂(200) with $d = 2.89$ Å. Further increasing the duration to 150 ms resulted in the formation of only crystalline nanoparticles (Fig. 3e, Supplementary Fig. 30). The interplanar spacing of $d = 2.11$ Å was attributed to NiPt(111). The elemental maps displayed a uniform distribution of Ni and Pt within the nanoparticle (Fig. 3e), indicating the formation of NiPt alloy crystal nanoparticles at the 150-ms duration.

To explain the critical role of FCR time, we recorded the real-time temperature under different FCR durations (Fig. 3f). The reaction duration determines the cooling rate, which reached $>10^4$ K s⁻¹ for 50 ms, but drop to $<10^3$ K s⁻¹ for 100 and 150 ms (Fig. 3f, inset). According to the temperature-time-transformation diagram (Fig. 3g), the cooling rate determines the formation of the glassy phase. The cooling profile for 100- and 150-ms duration would intersect with the crystal nose, leading to the formation of crystal phases. As a control, with the same Pt-Ni-P precursors loading, the synthesis in a conventional tube furnace with a slow cooling rate of ~ 10 K min⁻¹ only produced crystalline nanoparticles (Supplementary Fig. 31). These control experiments explicitly demonstrate that the glassy nanoparticle synthesis is kinetically controlled by ultrafast cooling.

Apart from the cooling rate, the P content plays a significant role in GFA of the metal-metalloid alloy⁴¹. As the precursors have distinct decomposition temperatures and vapor pressures (Supplementary Table 1), the product stoichiometry deviates from the initial precursor loading.

With an increase in FCR time, the atomic ratio of P in the product was reduced while the Pt ratio was increased (Fig. 3h). For the 150-ms duration, the P content was reduced to ~0 at%, resulting in formation of crystalline PtNi alloy (Fig. 3e). As a control, FCR of Pt precursor or Pt-Ni precursors led to crystal Pt or PtNi nanoparticles, respectively (Supplementary Figs. 32-33), highlighting the critical role of P in glassy nanoparticle formation. The FCR duration as a critical parameter pertains to other MG compositions. For the Pd-Ni-P system, both the FCR at 100 ms (Supplementary Fig. 34) and the synthesis using a tube furnace (Supplementary Fig. 35) led to the formation of crystalline PdNiP nanoparticles.

Nanosize effect enhanced glass forming ability

Combining easily tunable precursor loading and ultrafast synthesis, the FCR provides access to a broad compositional space of MG. By combinatorial development, we synthesized a large library of ternary PdNiP nanoparticles, whose phases (crystalline or glassy) and compositions were determined by TEM and EDS, respectively (Fig. 4a). The Pd-Ni-P phase diagram revealed that ~54% of the nanoparticles formed a glassy phase, covering about 10 to 55 at% of P. In comparison, the compositions of ribbon MG⁴² and bulk MG³⁵ appear to lie close to P ~20 at% (Fig. 4a), which is rooted in the deep eutectic points at approximately Ni₈₀P₂₀ and Pd₈₀P₂₀. Therefore, the phase space of PdNiP MG at the nanoscale is substantially larger than its bulk counterpart, i.e., the nanosize effect enhances the glass forming ability.

The R_C determines whether the phase is crystalline or glassy under a specific cooling rate. The composition-dependent R_C was calculated for the Pd-Ni-P system using an empirical model⁴³ and a recently developed algorithm⁴⁴ (Fig. 4b; computational details in Supplementary Note 4). The R_C strongly correlates with the P content, with compositions of 20 to 70 at% of P having R_C

$<100 \text{ K s}^{-1}$ (Fig. 4b). For P content $<10 \text{ at\%}$ or $>80 \text{ at\%}$, the R_C surges to $>10^4 \text{ K s}^{-1}$. As the cooling rate of our FCR is on the order of 10^4 K s^{-1} (Fig. 1d), it affords the synthesis of PdNiP MGNP with P content as low as $\sim 10 \text{ at\%}$ (Fig. 4b). This is consistent with the experimental result, where crystalline phases form at P content $<10 \text{ at\%}$ (Fig. 4a).

To further explain the dimension-dependent GFA, *ab initio* molecular dynamics was implemented to explore the MG structure in both the nanoparticulate and bulk forms. We modeled a PdNiP nanoparticle surrounded by a vacuum layer (Fig. 4c) and a PdNiP supercell under periodic boundary conditions (Fig. 4d), both having the same composition ratio (Pd:Ni:P $\sim 2:2:1$). While both ensembles had amorphous atomic structures, the local bond orientational order was employed to quantitatively describe the degree of disorder (see details in Methods)^{7,45}. 100% of the atoms in the MG nanoparticle are disordered under the normalized bond orientational order parameters criterion (Fig. 4e). In contrast, while most atoms ($\sim 96.4\%$) in the MG bulk are disordered, some have crystal features approaching hexagonal close packed (hcp) or face cubic center (fcc) structures (Fig. 4f). These results demonstrate that, even with the same composition, the MG nanoparticle is more disordered than its bulk counterpart, echoing the experimental observation that the nanosize effect enhances GFA. A series of MG with P content of ~ 11 , ~ 19 , ~ 33 , ~ 40 , and $\sim 52 \text{ at\%}$ were modeled (Supplementary Fig. 36), and the corresponding local bond orientational order shows that all the nanoparticles are more disordered than the bulk counterparts, regardless of the composition (Supplementary Fig. 37).

Furthermore, the subtle differences in short-range order between nanoscale and bulk MG were analyzed based on Voronoi tessellation^{7,41,46}. In metal-metalloid MG, the metals (Ni, Pd) and metalloid (P) exhibit distinct local orders⁴¹. The ten most prevalent Ni/Pd-centered Voronoi polyhedra in MG nanoparticle are depicted in Fig. 4g. Common motifs observed in MG, such as

distorted icosahedra with indices of $\langle 0, 1, 10, 2 \rangle$, $\langle 0, 2, 8, 2 \rangle$ and $\langle 0, 2, 8, 1 \rangle$, and $\langle 0, 3, 6, 3 \rangle$, are identified (Fig. 4h). For the P-centered cases (Fig. 4i), frequently encountered polyhedra include tricapped trigonal prisms with an index of $\langle 0, 3, 6, 0 \rangle$, and distorted tricapped trigonal prisms with indices of $\langle 0, 4, 4, 0 \rangle$, $\langle 0, 5, 2, 0 \rangle$, and $\langle 0, 3, 6, 1 \rangle$ (Fig. 4j). The Voronoi polyhedra of the MG bulk are mostly the same as those in the nanoparticle (Supplementary Fig. 38). The polyhedral face distribution of all the Voronoi polyhedra shows the most prevalent 5-edged Ni/Pd-centered faces in both MG nanoparticle and bulk. In contrast, the 4-edged P-centered polyhedral faces are the most abundant in MG nanoparticle, and 5-edged ones in MG bulk (Supplementary Fig. 39). Moreover, the coordination numbers of all the atoms in the MG were determined based on the Voronoi index from $\sum_i n_i$ (Figs. 4k-l). The average first-neighbor coordination numbers of Ni/Pd in MG nanoparticle (~ 11.5) are very similar to those of MG bulk (~ 11.1). However, the average coordination numbers of P in MG nanoparticle (7.9) are significantly smaller than those in MG bulk (8.8), clearly revealing the more disordered local structure of MG in nanoparticle form.

The conclusion of the enhanced GFA resulting from the nanosize effect has two immediate implications. First, for a given alloy system, a composition ratio that cannot form bulk MG may glassy material at the nanoscale. The strict composition requirement for bulk MG formation would be lessened for bottom-up nanoscale MG synthesis. Secondly, an alloy system that is inaccessible for bulk MG may form MG at the nanoscale. Based on this, we further expanded the Pd-based MG to compositions of Pd-Co-P (Supplementary Fig. 40), Pd-Sn-P (Fig. 2m, Supplementary Fig. 41), and high-entropy Pd-Cu-Ni-Fe-P (Fig. 4n, Supplementary Fig. 42), which, to the best of our knowledge, have not yet been synthesized in bulk form. This will inspire researchers to explore a wide range of glassy materials beyond current reports.

Catalytic applications of the metallic glass nanoparticles

The FCR enables the scalable and rapid production of uniformly dispersed MGNP with diverse elemental compositions, making them promising for a wide range of applications. We here demonstrated the ternary PtNiP MGNP as a high-performance electrocatalyst for hydrogen evolution reaction (HER). The choice of PtNiP over other MG compositions was determined after performance screening (Supplementary Fig. 43). HER activity was evaluated using a standard three-electrode setup in a N₂-saturated 0.5 M H₂SO₄ solution with rotation disc electrode (RDE). The optimized P content in the PtNiP catalysts was ~10% (Supplementary Fig. 44). Crystalline PtNi NP and high-quality commercial Pt/C were used as references. Polarization curves (Fig. 5a) indicate that the PtNiP MGNP has a very low overpotential (η) of ~14 mV to deliver 10 mA cm⁻², lower than those of PtNi NP (~22 mV) and Pt/C (~21 mV). We further compared the mass activities normalized to Pt loading (Supplementary Fig. 45, Supplementary Table 4). At $\eta = 50$ mV, PtNiP MGNP exhibits a mass activity of 11.6 A mg⁻¹_{Pt}, which is ~1.9 times and ~5.1 times higher than those of PtNi NP (6.11 mg⁻¹_{Pt}) and Pt/C (2.26 mg⁻¹_{Pt}), respectively. Additionally, PtNiP MGNP has a Tafel slope of only 18 mV dec⁻¹ (Fig. 5b), superior to Pt/C (21 mV dec⁻¹), suggesting the dominant Volmer-Tafel mechanism with recombination of chemisorbed H* as the rate-determining step⁴⁷. Considering the overpotential and Tafel slope, PtNiP MGNP is among the best precious metal-based catalysts reported recently (Fig. 5c, Supplementary Table 5).

We then explored the origin of the superior HER performance of PtNiP MGNP. First, the electrochemically active surface area (ECSA) was determined based on electrochemical double-layer capacitance (C_{dl}) measurement (Supplementary Fig. 46, Supplementary Table 6). Although PtNiP MGNP exhibits better HER activity, its ECSA is smaller than that of Pt/C, indicating that the difference in active surface area is not the primary reason for the superior catalytic performance.

Secondly, the turnover frequency (TOF) per active site was measured to evaluate the intrinsic catalytic ability (Supplementary Figs. 47-48). The TOF values for PtNiP MGNP at 20 mV and 50 mV (*vs* RHE) are 6.71 and 40.5 H₂ s⁻¹, respectively, significantly higher than those of Pt/C (0.22 H₂ s⁻¹ at 20 mV; 5.84 H₂ s⁻¹ at 50 mV), and represent one of the best results among Pt-group metal based nanocatalysts (Supplementary Fig. 48). Thirdly, the electrode kinetics for proton reduction was investigated by electrochemical impedance spectroscopy under η of 20 mV. The Nyquist plots show that the PtNiP exhibits a charge transfer resistance of $\sim 13 \Omega$, smaller than that of Pt/C at 21 Ω (Supplementary Fig. 49), demonstrating a fast Faradaic process at the interface between electrolyte and catalysts. Therefore, the excellent HER performance of PtNiP MGNP originates from its intrinsically high activity.

Stability is critical for practical applications. We first investigated the durability of the catalysts on RDE. The accelerated cyclic voltammetry aging test and chronopotentiometry measurement demonstrated negligible performance loss of PtNiP MGNP, which is comparable to Pt/C and outperforms crystalline PtNi NP (Supplementary Fig. 50). Post-catalysis characterizations suggest that the structure, size, and properties were well retained (Supplementary Figs. 51-52), demonstrating the robust stability of PtNiP MGNP in an acidic medium. Furthermore, to show the practical application potential of our PtNiP MGNP catalyst for clean H₂ production via water electrolysis, we constructed a proton exchange membrane water electrolyzer (PEM-WE) by using PtNiP MGNP in cathode. The *I-V* curve shows that PtNiP MGNP based PEM-WE needs 1.85, 2.06, and 2.45 V to drive 250, 500 and 1000 mA cm⁻² water electrolysis current density without *i-R* compensation (Fig. 5d). The performance of PtNiP MGNP based PEM-WE can be further improved by decreasing the cell resistance, which is $\sim 0.7 \Omega \text{ cm}^{-2}$. Importantly, the PtNiP MGNP based PEM-WE can operate with stability for 100 h at 250 mA cm⁻² without any sign of

increase in cell voltage (Fig. 5e). The PtNiP-based cell also operated well at an industrial-level current density of 1000 mA cm⁻² for 25 h (Supplementary Fig. 53). These performance tests clearly demonstrate the application potential of PtNiP MGNP in practical PEM-WE devices.

To explore the underlying structural factors contributing to the electrocatalytic performance, we employed extended X-ray absorption fine spectroscopy (EXAFS) to examine the coordination environment of PtNiP MGNP. The EXAFS of Pt *L*₃ edge revealed the presence of Pt-Pt, Pt-Ni, and Pt-P bonds in the PtNiP MGNP (Fig. 5f, Supplementary Table 7), while the Ni *K*-edge spectra showed the presence of Ni-Pt, Ni-Ni, and Ni-P (Supplementary Fig. 54, Supplementary Table 8). This shows the existence of various coordination environments for Pt and Ni species, a characteristic feature of a disordered structure. The coordination numbers of Ni and Pt in PtNiP MGNP are notably smaller than those in crystalline PtNi NP (Supplementary Tables 7-8), due to their bonding with P. Moreover, we found that the P is inclined to coordinate with Ni rather than Pt (Fig. 5f, Supplementary Fig. 54c), which finely tuned the electronic structure of Pt.

To further elucidate the mechanism dominating the HER performance, we calculated the Gibbs free energy of hydrogen adsorption (ΔG_{H}), where catalysts with ΔG_{H} near 0 eV are optimal. By combining molecular dynamics and structure optimization, we searched for surface structures of PtNiP MG with various compositions and obtained hydrogen adsorbed models (Supplementary Figs. 55-56, Supplementary Table 9). The ΔG_{H} of Pt(111) and PtNi(111) are comparable, indicating that alloying Pt with Ni does not significantly alter the hydrogen interaction (Fig. 5g). In striking contrast, adding P to the alloy qualitatively tunes the interaction: as P content increases, hydrogen binding weakens. The ΔG_{H} values of Pt₂Ni₂P₁ (P ~ 20 at%) and Pt₄Ni₄P₁ (P ~ 11 at%), are closer to 0 eV than Pt(111), agreeing well with the experimentally optimized P content (Supplementary Fig. 44). Moreover, the density of states (DOS) of the *d* orbitals of PtNiP MG is

shifted to the left compared to Pt(111) (Fig. 5h). The d -band center (ϵ_d) of Pt atoms in Pt₄Ni₄P₁ is further away from the Fermi level than that of Pt(111) by -0.14 eV, resulting in a weaker binding to H*. These findings explain the high intrinsic HER activity of PtNiP MGNP.

In addition to electrocatalysis, we extended the application of MGNG to heterogeneous catalysis (Supplementary Note 5), exemplified by Suzuki-Miyaura coupling (Supplementary Table 10) and Miyaura-Heck coupling (Supplementary Table 11). The PdNiP MGNP exhibits a higher TOF than crystalline PdNi NP in the catalytic coupling of a boronic acid and an aryl halide (Supplementary Table 10). Due to the versatility of our developed FCR method, the synthesized MGNP may find wide applications in various fields.

Conclusion

In conclusion, we developed a kinetically controlled FCR featuring with ultrafast heating and cooling for the general synthesis of Pd- and Pt-based MGNP with good control over their composition, particle size, dispersity, and supporting substrates. We discovered that the nanoscale MG has a expanded phase space than its bulk counterpart, indicating the nanosize effect enhanced GFA, which could inspire exploration of the compositional space of nanoscale MG beyond the bulk form. The MGNP show promising performance in electrocatalysis and heterogeneous catalysis. We anticipate that this method can be extended to synthesize a wide range of amorphous and metastable materials, thereby expanding the current crystal phase diagram dominated materials discovery.

Methods

Materials. Metal salts, including H_2PtCl_6 (≥ 37.5 wt% Pt basis, Millipore-Sigma), PdCl_2 (99 wt%, Aldrich Chem), CuCl_2 (97 wt%, Sigma-Aldrich), NiCl_2 (98 wt%, Sigma-Aldrich), FeCl_3 (Fisher Scientific), $\text{CoCl}_2 \cdot 6\text{H}_2\text{O}$ (Acros Organics), and $\text{SnCl}_4 \cdot 2\text{H}_2\text{O}$ (98 wt%, Sigma-Aldrich), were used as metal precursors. Triphenylphosphine (PPh_3 , 99 wt%, Acros Organics) was used as the phosphorus precursor. Carbon black (Carbot, Vulcan XC72) or carbon nanotubes (CNT, MEIJO DIPS, Single-Walled CNT) was used as conductive additives and supports.

Precursors loading. The metal precursors were dissolved in ethanol separately at a concentration of 0.05 M (Supplementary Fig. 1a). PdCl_2 was dissolved in ethanol with 1 M HCl. The loading of Pd or Pt was fixed to 5 wt% with respect to carbon black. Then, the amount of other precursors, including Cu, Ni, Fe, Co, Sn, and P, was calculated according to a fixed molar ratio. For example, in the synthesis of ternary PdNiP MGNP, we used the molar ratio of Pd:Ni:P = 1:1:2. Accordingly, the mass or volume for each precursor was carbon black (50 mg), PdCl_2 (0.05 M, 0.94 mL), NiCl_2 (0.05 M, 0.94 mL), and PPh_3 (0.05 M, 1.88 mL). The metal precursor solutions (PdCl_2 and NiCl_2) were mixed first, and then carbon black was added into the mixed solution. The slurry of carbon black and precursor solution was bath-sonicated (Cole-Parmer Ultrasonic Cleaner) for 10 min to enhance the dispersion, and then dried in a vacuum desiccator overnight (Supplementary Fig. 1b). Next, the black power was added to the PPh_3 solution, followed by sonication, and drying in a vacuum desiccator overnight. It is crucial to follow the above sequence, i.e., first loading metal precursors and then P precursor, to prevent the reaction of Pd^{2+} with PPh_3 and form a complex that precipitates in the ethanol. The same protocol also prevents the formation of PtCl_4^{2-} and PPh_3

complexes. The detailed precursor loading conditions for the synthesis of each MGNP, as well as the controlled samples, are listed in Supplementary Table 2.

FCR system and synthesis process. The electrical diagram of the FCR system is presented in Supplementary Fig. 3a. A mixture of carbon black and metal precursors were loaded into a quartz tube with an inner diameter of 4 mm. Graphite rods were used as the electrodes on both sides of the quartz tube. The quartz tube was set in a reaction jig and connected to the FCR system. The resistance of the sample was controlled by compressing the two electrodes. The reaction jig was placed inside a desiccator filled with Ar gas to prevent sample oxidation. The capacitor bank with total capacitance of 60 mF was charged by a DC supply capable of reaching 400 V. The discharging time was controlled by a relay with programmable delay time, accurate to millisecond. The specific parameters for synthesizing the various MGNP are listed in Supplementary Table 2. After the reaction, the samples rapidly cooled to room temperature.

Temperature Measurement. The temperature measurement was performed using an IR thermometer (Micro-Epsilon) with a temperature range of 200 to 1500 °C. The thermometer was connected to LabView through a Multifunction I/O (NI USB-6009) for real-time temperature recording with time resolution of 0.1 ms. Before use, the temperature was calibrated.

Characterization. SEM images were obtained using a FEI Quanta 400 ESEM Field Emission Microscope at 5 kV. EDS spectra were collected using the same system equipped with an EDS detector at 30 kV. XPS spectra were acquired on a PHI Quantera XPS system under a pressure of 5×10^{-9} Torr. Full XPS spectra were acquired with a step size of 0.5 eV and a pass energy of 140

eV, and elemental XPS spectra were acquired with a step size of 0.1 eV and a pass energy of 26 eV. All XPS spectra were calibrated using the standard C 1s peak at 284.8 eV. XRD was conducted on a Rigaku SmartLab XRD using Cu K α radiation ($\lambda = 1.5406 \text{ \AA}$). BF-TEM, HRTEM, and tilt-angle HRTEM images were collected using a JEOL 2100 field emission gun transmission electron microscope operating at 200 kV. SAED and nanobeam diffraction were collected using the same JEOL 2100F TEM system, and the diffraction patterns were calibrated using the Al standard. HAADF-STEM imaging and EDS mapping were carried out on a FEI Titan Themis3 system equipped with image and probe aberration corrections and an electron monochromator operating at 80 kV.

Ab initio molecular dynamics (MD) simulation of atomic structures of PdNiP MG. The density functional theory (DFT) method⁴⁸ implemented in the Vienna *ab initio* simulation package (VASP)⁴⁹ was used. A plane wave expansion up to 500 eV was employed in combination with an all-electron-like projector augmented wave potential⁵⁰. Exchange-correlation was treated within the generalized gradient approximation using the functional parameterized by Perdew and Wang⁵¹. Both bulk MG and their nanoparticle counterparts with the same composition were studied using the same method, potentials, and criteria of convergence for electronic band and atomic forces. The initial coordinates of atoms were generated using a random number generator with the constraint that all the atoms were closely packed in a box for bulk or a sphere for nanoparticle based on their bond lengths. Bulk MG was modeled in a supercell containing 420 atoms with the size of the supercell optimized. Nanoparticle MG was modeled in a sphere containing 313 atoms surrounded by a 10–15 \AA thick vacuum layer. Since all the supercells are large enough, only Γ point was used for the Brillouin zone integration over a Monkhorst-Pack type mesh⁵². For structure

optimization, the atoms were considered fully relaxed when the maximum force on each atom is smaller than $0.01 \text{ eV } \text{\AA}^{-1}$. The optimized structures were then annealed at $\sim 1500 \text{ K}$ in a MD simulation, followed by rapid cooling to 300 K at a rate of 125 K ps^{-1} . The MD simulations were performed using Nose-Hoover thermostat and number-volume-temperature (NVT) ensemble. The resulting atomic structures were then optimized, as shown in Supplementary Fig. 36.

Local bond orientational order (BOO) parameters. Local BOO parameters (Q_4 and Q_6) were calculated from the atomic models of both MG bulks and MG nanoparticles obtained by MD simulation, using the method described previously^{7,45}. The distribution of the local BOO parameter for all the atoms in bulks and particles are shown in Figs. 4e-f and Supplementary Fig. 37. A normalized BOO parameter is defined as $\sqrt{Q_4^2 + Q_6^2} / \sqrt{Q_{4,\text{fcc}}^2 + Q_{6,\text{fcc}}^2}$, where $Q_{4,\text{fcc}}$ and the $Q_{6,\text{fcc}}$ are the Q_4 and Q_6 parameters for perfect fcc structures⁷. This normalized parameter is between 0 and 1, where a larger value represents a more ordered structure. A normalized parameter value of 0.5 is used as the cut-off to separate the amorphous and ordered structures. The fraction of disordered atoms in the metallic glass was calculated (Supplementary Fig. 37k).

Short-range order analysis based on Voronoi tessellation and the coordination number. The Voronoi analysis of each atomic model of metallic glass was conducted by following a recent report⁷. The regulation was applied to each Voronoi polyhedron that those surfaces with areas less than 1% of the total polyhedron surface area were removed to minimize the degeneracy problem and thermal vibration effects⁴⁶. Each polyhedron was assigned an Voronoi index, $\langle n_3, n_4, n_5, n_6, \dots \rangle$, where n_i represent the number of i -edged faces of the polyhedron. After obtaining the Voronoi index, the coordination number (CN) of the center atom was calculated from $\sum_i n_i$.

References

- 1 Klement, W., Willens, R. H. & Duwez, P. Non-crystalline structure in solidified gold-silicon alloys. *Nature* **187**, 869-870 (1960).
- 2 Greer, A. L. Metallic glasses...on the threshold. *Materials Today* **12**, 14-22 (2009).
- 3 Li, M. X. *et al.* High-temperature bulk metallic glasses developed by combinatorial methods. *Nature* **569**, 99-103 (2019).
- 4 Ding, S. Y. *et al.* Combinatorial development of bulk metallic glasses. *Nature Materials* **13**, 494-500 (2014).
- 5 Kui, H. W., Greer, A. L. & Turnbull, D. Formation of bulk metallic-glass by fluxing. *Applied Physics Letters* **45**, 615-616 (1984).
- 6 Chen, M. A brief overview of bulk metallic glasses. *NPG Asia Materials* **3**, 82-90 (2011).
- 7 Yang, Y. *et al.* Determining the three-dimensional atomic structure of an amorphous solid. *Nature* **592**, 60-64 (2021).
- 8 Kiani, M. T. *et al.* Ductile metallic glass nanoparticles via colloidal synthesis. *Nano Lett.* **20**, 6481-6487 (2020).
- 9 Sha, Z. D. *et al.* Notch strengthening in nanoscale metallic glasses. *Acta Materialia* **169**, 147-154 (2019).
- 10 Jang, D. & Greer, J. R. Transition from a strong-yet-brittle to a stronger-and-ductile state by size reduction of metallic glasses. *Nature Materials* **9**, 215-219 (2010).
- 11 Shen, Y. Y., Li, Y. Q., Chen, C. & Tsai, H. L. 3D printing of large, complex metallic glass structures. *Materials & Design* **117**, 213-222 (2017).
- 12 Kumar, G., Tang, H. X. & Schroers, J. Nanomoulding with amorphous metals. *Nature* **457**, 868-872 (2009).

- 13 Glasscott, M. W. *et al.* Electrosynthesis of high-entropy metallic glass nanoparticles for designer, multi-functional electrocatalysis. *Nat. Commun.* **10**, 2650 (2019).
- 14 Li, J. Y., Doubek, G., McMillon-Brown, L. & Taylor, A. D. Recent advances in metallic glass nanostructures: Synthesis strategies and electrocatalytic applications. *Adv. Mater.* **31**, 1802120-1802147 (2019).
- 15 Hu, Y. C. *et al.* A highly efficient and self-stabilizing metallic-glass catalyst for electrochemical hydrogen generation. *Adv. Mater.* **28**, 10293-10297 (2016).
- 16 Carmo, M. *et al.* Bulk metallic glass nanowire architecture for electrochemical applications. *Acs Nano* **5**, 2979-2983 (2011).
- 17 Gao, F.-Y. *et al.* Nickel–molybdenum–niobium metallic glass for efficient hydrogen oxidation in hydroxide exchange membrane fuel cells. *Nat. Catal.* **5**, 993-1005 (2022).
- 18 Kumar, G., Desai, A. & Schroers, J. Bulk metallic glass: The smaller the better. *Adv. Mater.* **23**, 461-476 (2011).
- 19 Yan, W. *et al.* Structured nanoscale metallic glass fibres with extreme aspect ratios. *Nat. Nanotechnol.* **15**, 875-882 (2020).
- 20 Wada, T., Louzguine-Luzgin, D. V. & Inoue, A. Preparation of Zr-based metallic glass nanowires and nanoparticles by selective etching. *Scripta Materialia* **57**, 901-904 (2007).
- 21 Liang, S.-X. *et al.* A laser-based synthesis route for magnetic metallic glass nanoparticles. *Scripta Materialia* **203**, 114094-114099 (2021).
- 22 Ma, Y. *et al.* Amorphous PtNiP particle networks of different particle sizes for the electro-oxidation of hydrazine. *RSC Advances* **5**, 68655-68661 (2015).

- 23 Zhao, M., Abe, K., Yamaura, S., Yamamoto, Y. & Asao, N. Fabrication of Pd-Ni-P metallic glass nanoparticles and their application as highly durable catalysts in methanol electro-oxidation. *Chemistry of Materials* **26**, 1056-1061 (2014).
- 24 Wang, W. *et al.* General synthesis of amorphous PdM (M = Cu, Fe, Co, Ni) alloy nanowires for boosting HCOOH dehydrogenation. *Nano Lett.* **21**, 3458-3464 (2021).
- 25 Zeeshan, M. A. *et al.* Electrochemically synthesized amorphous and crystalline nanowires: dissimilar nanomechanical behavior in comparison with homologous flat films. *Nanoscale* **8**, 1344-1351 (2016).
- 26 Liu, Y. H. *et al.* Metallic glass nanostructures of tunable shape and composition. *Nat. Commun.* **6**, 7043 (2015).
- 27 Yao, Y. *et al.* Carbothermal shock synthesis of high-entropy-alloy nanoparticles. *Science* **359**, 1489-1494 (2018).
- 28 Yao, Y. *et al.* Computationally aided, entropy-driven synthesis of highly efficient and durable multi-elemental alloy catalysts. *Sci. Adv.* **6**, eaaz0510 (2020).
- 29 Cui, M. *et al.* Multi-principal elemental intermetallic nanoparticles synthesized via a disorder-to-order transition. *Sci. Adv.* **8**, eabm4322 (2022).
- 30 Wang, B. *et al.* General synthesis of high-entropy alloy and ceramic nanoparticles in nanoseconds. *Nat. Synth.* **1**, 138-146 (2022).
- 31 Johnson, W. L. *et al.* Beating crystallization in glass-forming metals by millisecond heating and processing. *Science* **332**, 828-833 (2011).
- 32 Butland, A. T. D. & Maddison, R. J. The specific heat of graphite: An evaluation of measurements. *J. Nucl. Mater.* **49**, 45-56 (1973).

- 33 Chen, H. S. Glass temperature, formation and stability of Fe, Co, Ni, Pd and Pt based glasses. *Materials Science and Engineering* **23**, 151-154 (1976).
- 34 Chen, H. S. Composition dependence of the glass transition temperatures of Pd-Ni-P and Pt-Ni-P glasses. *Journal of Non-Crystalline Solids* **12**, 333-338 (1973).
- 35 He, Y. & Schwarz, R. B. Synthesis and properties of bulk metallic glasses in Pd-Ni-P and Pd-Cu-P alloys. *MRS Proceedings* **455**, 495-500 (1996).
- 36 Lan, S. *et al.* Hidden amorphous phase and reentrant supercooled liquid in Pd-Ni-P metallic glasses. *Nat. Commun.* **8**, 14679 (2017).
- 37 Bordeenithikasem, P. *et al.* Determination of critical cooling rates in metallic glass forming alloy libraries through laser spike annealing. *Scientific Reports* **7**, 7155 (2017).
- 38 Schwarz, R. B. & He, Y. in *Properties of Complex Inorganic Solids* (eds Antonios Gonis, Annemarie Meike, & Patrice E. A. Turchi) 287-299 (Springer US, 1997).
- 39 Takeuchi, A. *et al.* Pd₂₀Pt₂₀Cu₂₀Ni₂₀P₂₀ high-entropy alloy as a bulk metallic glass in the centimeter. *Intermetallics* **19**, 1546-1554 (2011).
- 40 Duan, Y. J. *et al.* Analysis of the anelastic deformation of high-entropy Pd₂₀Pt₂₀Cu₂₀Ni₂₀P₂₀ metallic glass under stress relaxation and recovery. *Journal of Materials Science & Technology* **107**, 82-91 (2022).
- 41 Guan, P. F., Fujita, T., Hirata, A., Liu, Y. H. & Chen, M. W. Structural origins of the excellent glass forming ability of Pd₄₀Ni₄₀P₂₀. *Physical Review Letters* **108**, 175501-175505 (2012).
- 42 Schluckebier, G. & Predel, B. Investigations on demixing and crystallization behavior of metallic glasses of the system palladium-nickel-phosphorus. *Zeitschrift Fur Metallkunde* **74**, 569-576 (1983).

- 43 Takeuchi, A. & Inoue, A. Quantitative evaluation of critical cooling rate for metallic glasses. *Materials Science and Engineering A-Structural Materials Properties Microstructure and Processing* **304**, 446-451 (2001).
- 44 Gabski, M., Peterlechner, M. & Wilde, G. Exploring the phase space of multi-principal-element alloys and predicting the formation of bulk metallic glasses. *Entropy* **22**, 292 (2020).
- 45 Lechner, W. & Dellago, C. Accurate determination of crystal structures based on averaged local bond order parameters. *The Journal of Chemical Physics* **129**, 114707 (2008).
- 46 Sheng, H. W., Luo, W. K., Alamgir, F. M., Bai, J. M. & Ma, E. Atomic packing and short-to-medium-range order in metallic glasses. *Nature* **439**, 419-425 (2006).
- 47 Liu, D. *et al.* Atomically dispersed platinum supported on curved carbon supports for efficient electrocatalytic hydrogen evolution. *Nature Energy* **4**, 512-518 (2019).
- 48 Dudarev, S. L., Botton, G. A., Savrasov, S. Y., Humphreys, C. J. & Sutton, A. P. Electron-energy-loss spectra and the structural stability of nickel oxide: An LSDA+U study. *Phys Rev B* **57**, 1505-1509 (1998).
- 49 Kresse, G. & Furthmüller, J. Efficient iterative schemes for ab initio total-energy calculations using a plane-wave basis set. *Phys Rev B* **54**, 11169-11186 (1996).
- 50 Blochl, P. E. Projector augmented-wave method. *Phys Rev B* **50**, 17953-17979 (1994).
- 51 Perdew, J. P. & Wang, Y. Accurate and simple analytic representation of the electron-gas correlation energy. *Physical Review B* **45**, 13244-13249 (1992).
- 52 Monkhorst, H. J. & Pack, J. D. Special points for Brillouin-zone integrations. *Physical Review B* **13**, 5188-5192 (1976).

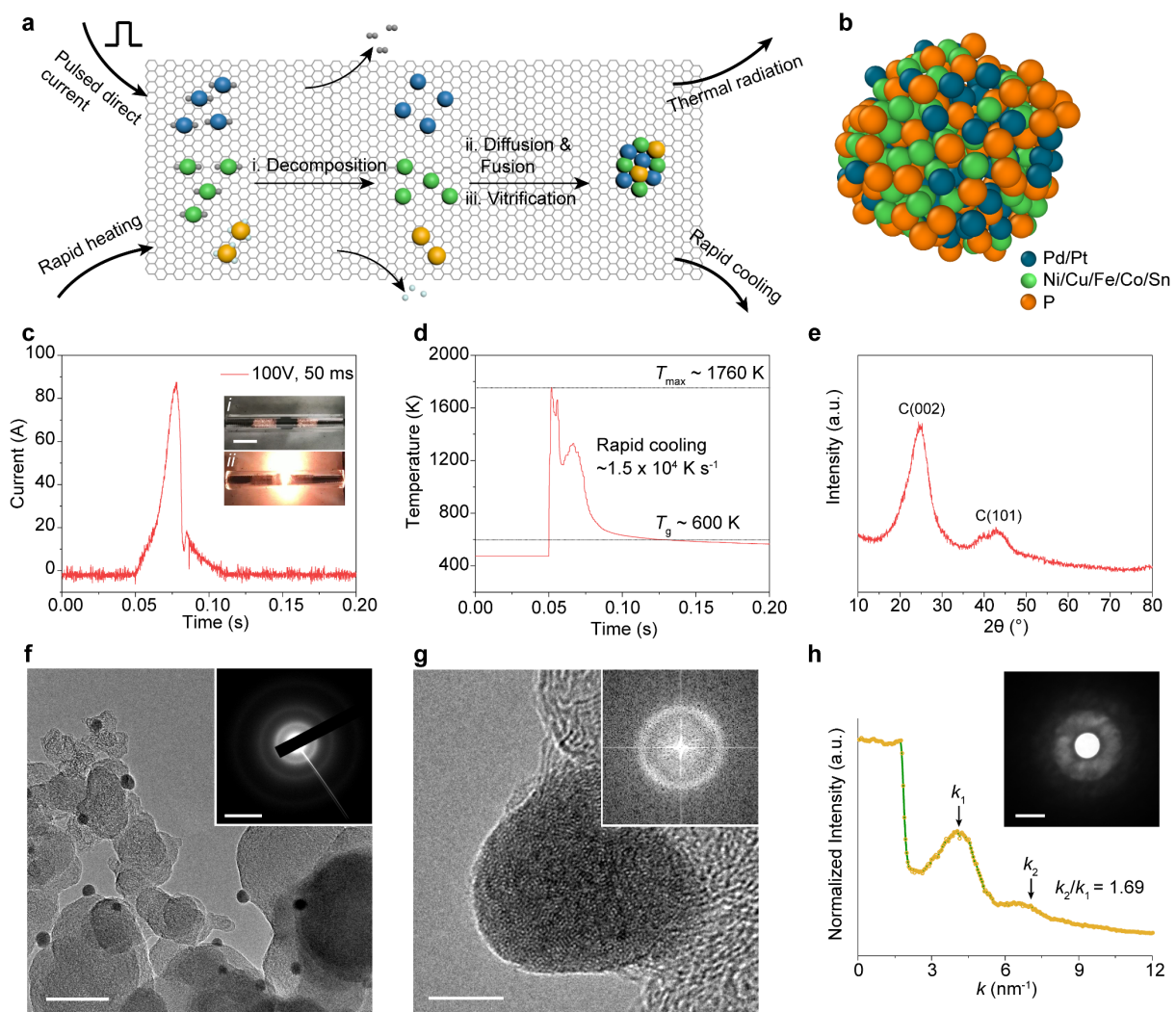


Fig. 1. Synthesis of PdNiP MGNP by flash carbothermic reaction. (a) Schematic of the FCR process for MGNP synthesis. (b) Molecular dynamics simulated atomic model of a ternary MGNP. (c) Pulsed current curve under the FCR conditions of 100 V and 50 ms. Inset, the pictures of the sample before (top) and during (bottom) the FCR reaction. (d) Real-time temperature curve recording using an infrared thermometer. T_{\max} and T_g are the maximum temperature of the FCR process and the glass transition temperature of PdNiP, respectively. (e) XRD pattern of the PdNiP MGNP supported on carbon black. The PDF reference card is graphite (PDF#41-1487). (f) BF-TEM image of the PdNiP MGNP supported on carbon black. Inset, SAED pattern of the MGNP

supported on carbon black. The scale bar is 50 nm for the TEM image, and 5 nm⁻¹ for the SAED pattern. **(g)** HRTEM image of the PdNiP MGNP and corresponding FFT image (inset). Scale bar, 5 nm. **(h)** Nanobeam diffraction pattern of the PdNiP MGNP, and the intensity profile derived from the electron diffraction. k_1 and k_2 are the first and second diffraction vectors, respectively. Scale bar, 5 nm⁻¹.

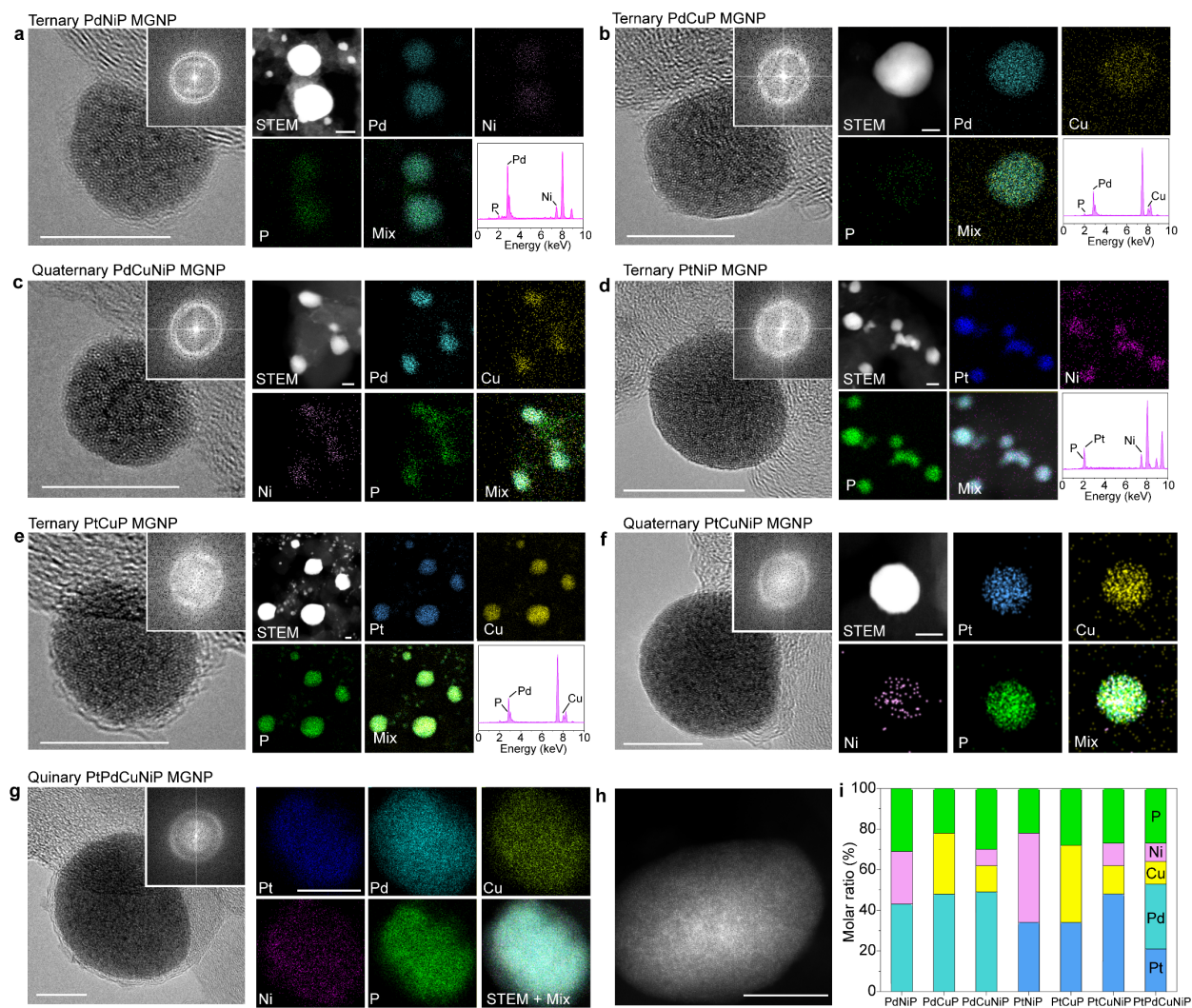


Fig. 2. General synthesis of MGNP by the FCR process. HRTEM images, corresponding FFT patterns, HAADF-STEM images, elemental maps, and EDS spectra for (a) ternary PdNiP MGNP, (b) ternary PdCuP MGNP, (c) quaternary PdCuNiP MGNP, (d) ternary PtNiP MGNP, (e) ternary PtCuP MGNP, (f) quaternary PtCuNiP MGNP, and (g) quinary, high-entropy PtPdCuNiP MGNP. (h) HAADF-STEM image of a PtPdCuNiP MGNP. All scale bars in the HRTEM images and STEM images are 10 nm. (i) Element molar ratio of MGNP.

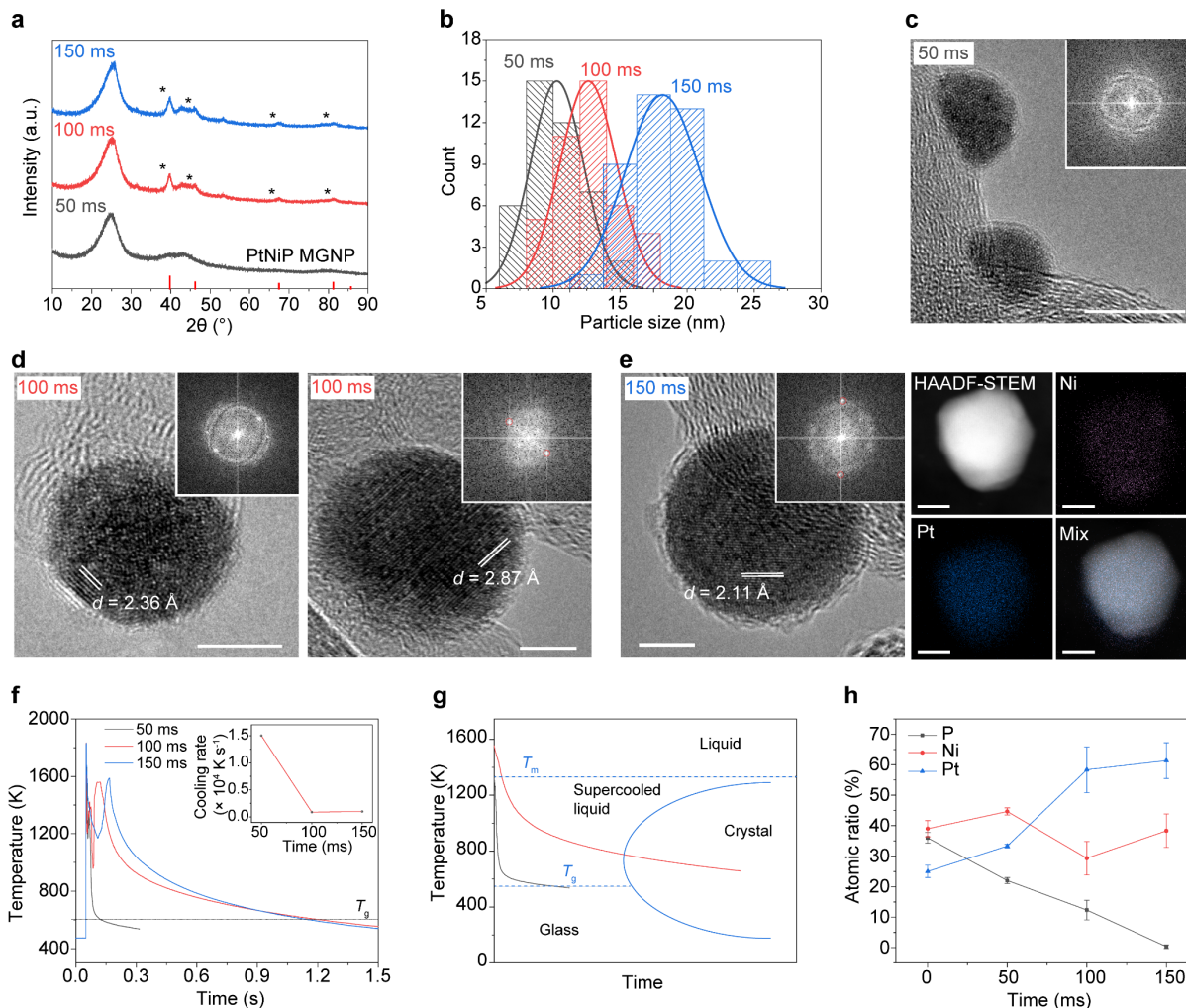


Fig. 3. Kinetically controlled synthesis of PtNiP MGNP. (a) XRD patterns of PtNiP synthesized under different FCR duration. The Pt reference is shown at the bottom axis (PDF#65-2868). (b) Particle size statistics and distribution of PtNiP NP synthesized under different FCR duration. (c) HRTEM image and corresponding FFT pattern (inset) of PtNiP MGNP synthesized at 50 ms. Scale bar, 5 nm. (d) HRTEM images and corresponding FFT patterns (inset) of NP synthesized at 100 ms. The lines show the lattice spacings. Scale bar, 5 nm. (e) HRTEM image, corresponding FFT pattern (inset), HAADF-STEM image, and elemental maps of the NP synthesized at 150 ms. The line shows the lattice spacing. Scale bar, 10 nm. (f) Real-time temperature curves under different FCR duration. Inset, the cooling rates of different FCR time. T_g is the glass transition temperature

of PtNiP. **(g)** Time-temperature-transformation diagram showing the kinetic formation of MG. T_m and T_g are the melting temperature and the glass transition temperature of PdNiP, respectively. **(h)** FCR time-dependent atomic ratios of P, Ni, and Pt in the synthesized NP.

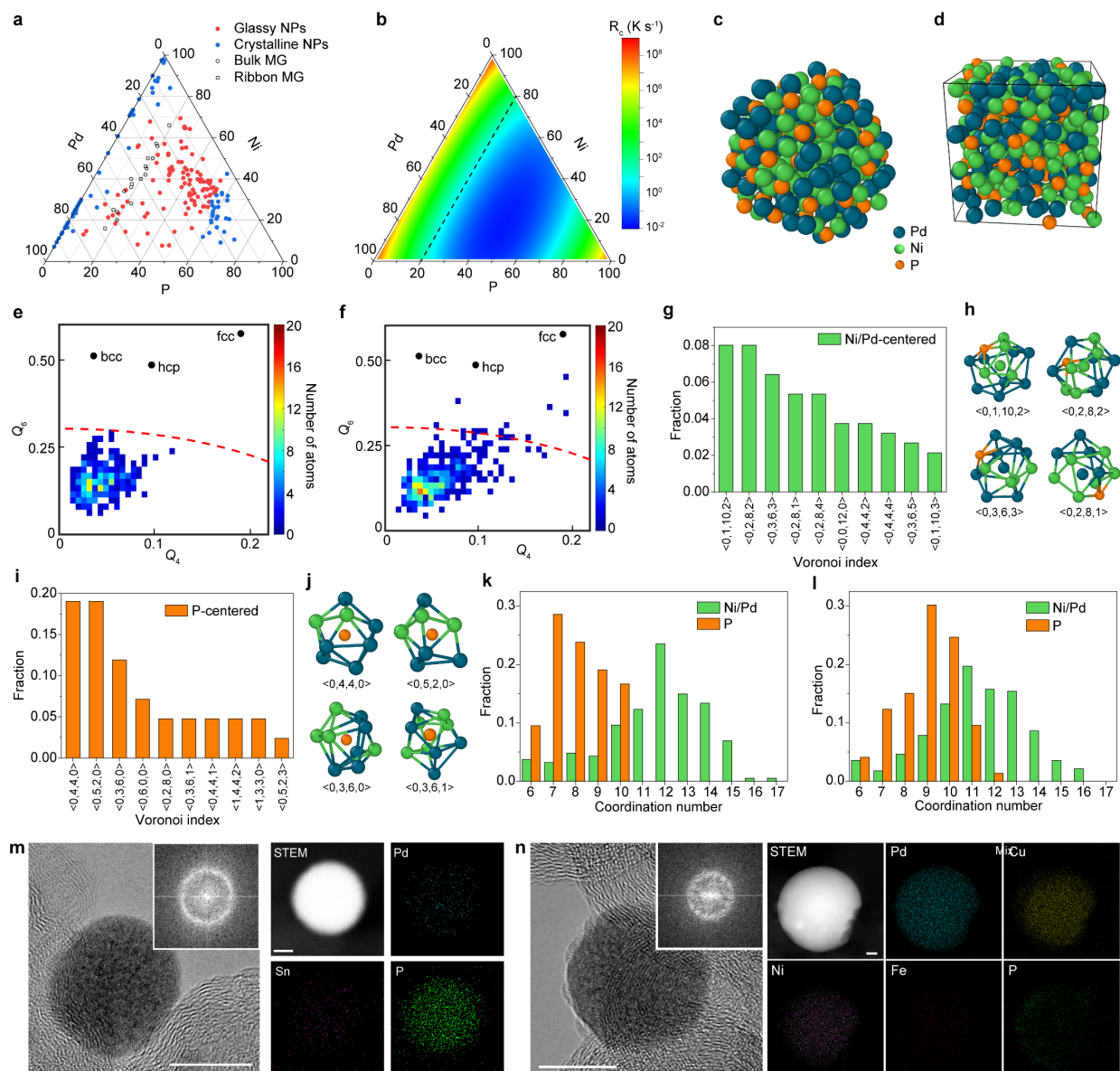


Fig. 4. Nanoscale effect enhanced glass forming ability. (a) The phase diagram of the ternary Pd-Ni-P system. The compositions of bulk MG and ribbon MG were from literatures values^{35,42}. (b) Calculated R_c of the ternary Pd-Ni-P system. The dash line denotes the composition of P = 20 at%. (c) Molecular dynamics simulated 3D atomic model of MG nanoparticle with composition of Pd₁₂₆Ni₁₂₇P₆₀ (P at% ~19%). (d) Molecular dynamics simulated 3D atomic model of MG bulk with composition of Pd₁₇₀Ni₁₇₀P₈₀ (P at% ~19%). (e-f) Local bond orientational order parameters of all

the atoms in the MG nanoparticle **(e)** and the MG bulk **(f)**. The dashed red curves denote the normalized bond orientational order parameter at 0.5, which serves as the criterion differentiating disordered and ordered structures. **(g)** Ten most abundant Ni/Pd-centered Voronoi polyhedra in the MG nanoparticle. **(h)** Four representative Ni/Pd-centered Voronoi polyhedra. **(i)** Ten most abundant P-centered Voronoi polyhedra in the MG nanoparticle. **(j)** Four representative P-centered Voronoi polyhedra. **(k)** The coordination number distribution of Ni/Pd and P for MG nanoparticle. The average coordination number of Ni/Pd and P are 11.5 and 7.9, respectively. **(l)** The coordination number distribution of Ni/Pd and P for MG bulk. The average coordination number of Ni/Pd and P are 11.1 and 8.8, respectively. **(m-n)** HRTEM image, the corresponding FFT pattern, HAADF-STEM image, and elemental maps of **(m)** PdCoP, and **(n)** high-entropy PdCuNiFeP MGNP. Scale bars, 10 nm.

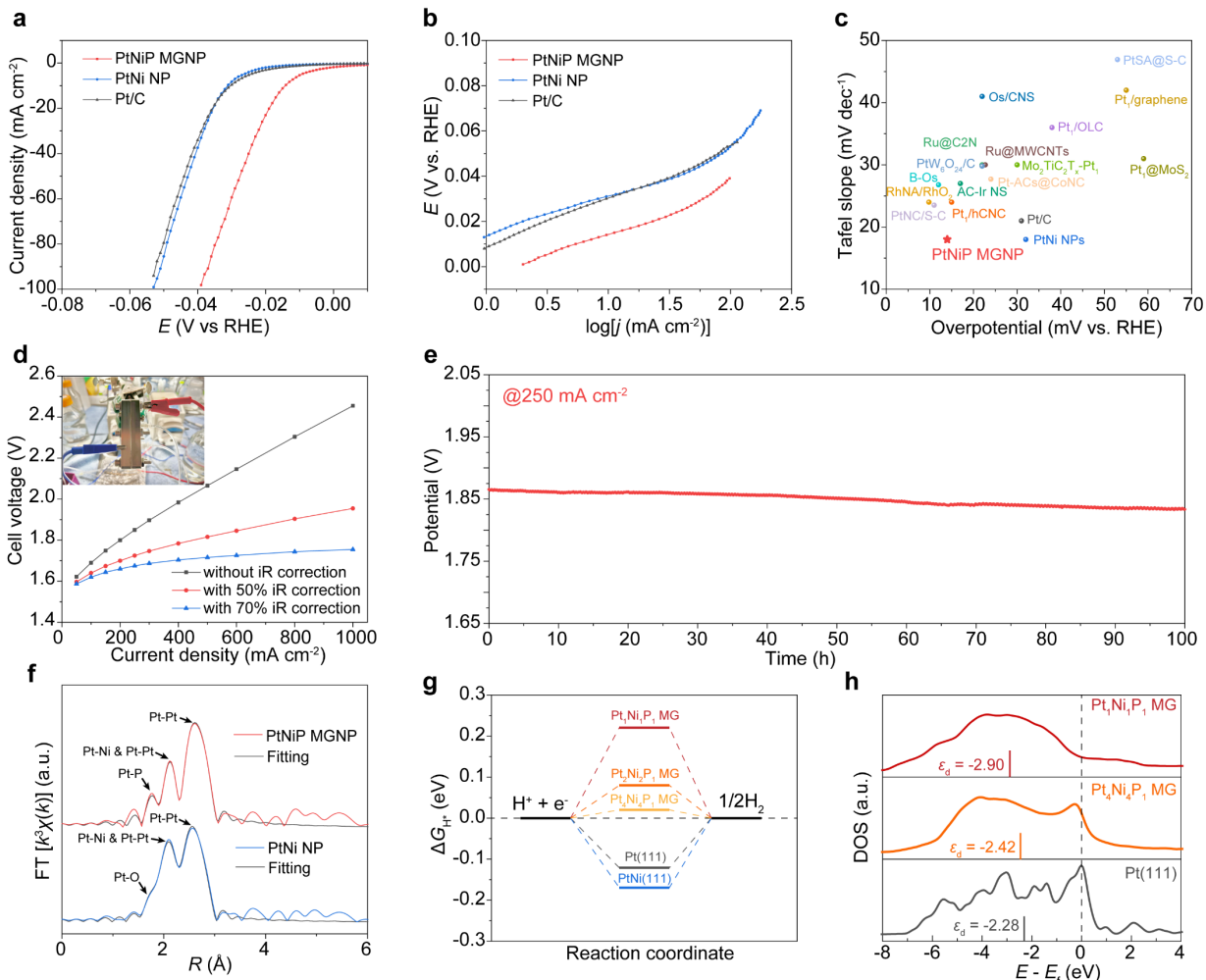


Fig. 5. Application of PtNiP MGNP in electrocatalytic hydrogen evolution. (a) Polarization curves of PtNiP MGNP, PtNi NP, and commercial Pt/C. **(b)** Tafel plots derived from the polarization curves. **(c)** Performance (overpotential at 10 mV dec⁻¹ and Tafel slope) comparison between this work and recent reported precious metal-based catalysts. The data and references are shown in Supplementary Table 5. All the measurements were conducted in 0.5 M H₂SO₄ by dropping the electrocatalysts on glassy carbon electrode using a three-electrode configuration. **(d)** Polarization curves of the PEM electrolyzer. Inset, photograph of the 1 cm² PEM electrolyzer test station. **(e)** Durability voltage-time plots for the PEM electrolyzer. **(f)** The Pt L₃ edge FT-EXAFS spectra and fitting results of PtNi NP and PtNiP MGNP. **(g)** Calculated free-energy diagram of

hydrogen adsorption at the equilibrium potential for Pt(111), PtNi(111), and PtNiP MG with different compositions. **(h)** The DOS of d orbitals of the active Pt on Pt(111), PtNi(111), and PtNiP MG. The d band center positions relative to the E_f were labeled.